Driving Force Control for On-board Motor Electric Vehicles with Adaptive Drivetrain Friction and Phase Stabilization Speed Controller

Yuki Hosomi[1], Binh-Minh Nguyen[1], Hiroshi Fujimoto[1], Hiroaki Ikeda[2], and Tatsuro Nohara[2]

Abstract— Driving force control (DFC) has been shown as a successful method for improving the safety and comfort of in-wheel-motor electric vehicles (IWM-EVs). However, DFC for on-board motor (OBM) EVs faces many challenges due to the complexity and parameter uncertainty of the powertrain system, which includes gear, differential, and drive shaft. Aiming to solve the aforementioned issues, this paper presents a new DFC system for OBM-EVs with the force controller in the outer loop, and the motor speed controller in the inner loop. To achieve phase stabilization, the proportional-integral-derivative (PID) controller with a phase lead compensator is proposed for the inner loop. By integrating disturbance observer and least square algorithm, a novel adaptive driving force observer (A-DFO) is proposed to simultaneously estimate the driving force and the viscous friction coefficient of the drivetrain. A hardware-in-the-loop (HIL) experiment is introduced to show that it is possible to design DFC for OBM-EVs using IEM-EVs. Numerical simulations and Hardware-in-loop experiments show that the proposed system can accurately estimate and control the driving force. Especially, the tracking errors and vibrations are remarkably reduced in comparison with some existing control approaches.

I. INTRODUCTION

The high environmental performance of electric vehicles has garnered significant attention with the progress of motor drive systems [1]. Recent advancements in energy estimation [2] and the range extension autonomous driving [3], [4] have mitigated the short mileage per charge, which is a weakness compared to hybrid electric vehicles[5]. Furthermore, in comparison to internal combustion engines, motors have a much faster torque response, and the actual torque can be accurately measured. These merits enable the development of advanced motion control such as chassis control [6] and vibration suppression [7]. The focus of this paper is safe and comfortable driving force generation for OBM-EVs.

Several related concepts have been proposed to safely generate the driving force for in-wheel-motor EVs (IWM-EVs). They are classified as anti-slip control (ASC) [8], slip ratio control (SRC) [9], and driving force control (DFC) [10]. ASC employs a disturbance observer-based controller. Due to its rough configuration, it is impossible for ASC to achieve the desired driving force accurately. On the other hand, SRC directly manipulates the slip ratio. It is hard to integrate ASC with other higher-layer motion controllers. Utilizing a

cascade configuration with force control in the outer-loop and motor speed control in the inner-loop, DFC can accurately track the driving force with the desired value. However, DFC has been mainly developed for IWM-EV.

Extending the DFC from IWM-EVs to OBM-EVs is a challenging task. In the case of IWM-EV, DFC design is straightforward due to the fact that the drivetrain can be modeled by an inertia term. As the inertia can be known precisely, the driving force can be estimated accurately from the motor torque, motor speed, and the disturbance observer [10]. Besides, good performance of the inner-loop can be attained even with a proportional-integral (PI) speed controller, the poles of the closed loop system can be placed at the desired position. In contrast, the drivetrain from a motor to tires of OBM-EVs is a complex plant, which is usually modeled as a two-inertia system [11], [12]. Generally, the resolution of the wheel speed sensor is smaller than the encoder of the motor, and it is necessary to estimate the driving force and control the speed using the motor angular speed. The plant is a third-order plant that takes inertias and frictions into account, and the pole arrangement cannot be done by a PI controller [11], so a higher-order controller is required. The bandwidth of the controller is limited by the resonance frequency of the plant, thus the feed-forward (FF) controller is used to reduce the tracking error in [11]. However, this method needs a precious nominal model. For driving force estimation, inertia alone cannot estimate the driving force. Loss due to viscous friction leads to an estimation error [11]. Other recent studies have not considered viscous friction or frequency response of the drivetrain of OBM-EVs when designing traction control [13], [14]. However, it is imperative to incorporate a comprehensive drive train model into the design.

To overcome the issues above, this paper focuses on adapting DFC to OBM-EV. Especially, the proposed controller improves the tracking performance of the speed controller and the estimation accuracy of the driving force observer (DFO) which are issues in [11]. As for a motor speed controller, the phase lead compensator is added to the conventional PI controller, and a high order controller with PID controller and phase lead compensator is proposed to increase a phase margin based on the frequency response obtained by the two-inertia model. Furthermore, to improve the accuracy of the driving force estimation, viscous friction is introduced into conventional DFO, and sequential estimation of both the viscous friction coefficient by recursive least square (RLS) and the driving force by the state observer is proposed. Finally, we show that IWM-EVs, which have an ideal drivetrain with no nonlinear components, are effective in designing DFC for

[1]Yuki Hosomi, Binh-Minh Nguyen, and Hiroshi Fujimoto are with Graduate School of Frontier Science, The University of Tokyo, 5-1-5, Kashiwanoha, Kashiwa, Chiba, 277-8561, Japan `fujimoto@k.u-tokyo.ac.jp`
[2]Hiroaki Ikeda and Tatsuro Nohara are with Development Division, Komatsu Ltd., 3-25-1 Shinomiya, Hiratsuka, Kanagawa 254-8555, Japan `tatsurou_nohara@global.komatsu`

(a) Vehicle model. (b) Drivetrain model.
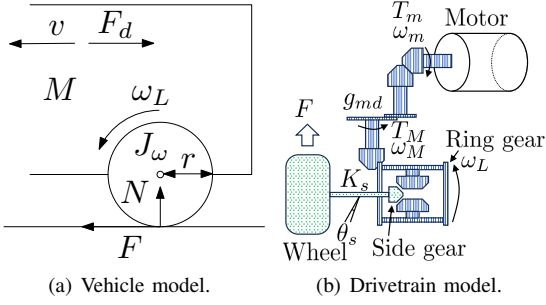
Fig. 1. OBM-EV Drivetrain with a differential gear and drive shafts.

Fig. 2. Drivetrain block diagram.

OBM-EVs. The proposed method is evaluated using a novel HIL experiment system, in which the IWM is regarded as the load side of the driveshaft, and other components are realized in the simulator. By the aforementioned approach, the controller design for any type of EVs can be performed using IWM-EVs.

II. Modeling

A. Vehicle dynamics

For the sake of simplicity, this study focuses on the longitudinal motion of the single-wheel vehicle model in Fig. 1(a) with the drivetrain shown in Fig. 1(b). A drive system is modeled in which the motor is connected to the tires by a reduction gear and a differential gear, and the decelerated output is distributed to the left and right by the differential gear and transmitted to the tires via the drive shafts. Taking into account the reduction ratio g_{md} of the reduction gear, the torque T_m and angular speed ω_m at the motor are converted to torque T_M and angular speed ω_M at the ring gear using the following equations

$$\omega_M = g_{md}\omega_m, \tag{1}$$

$$T_M = \frac{T_m}{g_{md}}. \tag{2}$$

The equations that describe the rotational motion of the motor and wheel are expressed as follows

$$J_M\dot{\omega}_M = T_M - B_M\omega_M - K_s\theta_s, \tag{3}$$

$$J_{L0}\dot{\omega}_L = K_s\theta_s - B_L\omega_L - rF, \tag{4}$$

$$\theta_s = \begin{cases} \theta_S - \theta_b & (\theta_S > \theta_b) \\ 0 & (-\theta_b \leq \theta_S \leq \theta_b) \\ \theta_S + \theta_{th} & (\theta_S < -\theta_b), \end{cases} \tag{5}$$

$$\theta_S = \int(\omega_M - \omega_L)dt, \tag{6}$$

where r, and K_s are the wheel radius, and driveshaft rigidity, respectively, and ω_M, ω_L, $J_M = J_m/g_{md}^2 + J_{\text{input}} + J_{\text{ring}} + J_{\text{pinion}}$, $J_{L0} = J_{side} + J_{drive} + J_\omega$, B_M, B_L are the sum of inertias of components, viscous friction coefficients, and angular speeds of both the drive side and load side, respectively. Equations (5) and (6) represent the backlash of the differential gear where θ_b is the boundary value of the
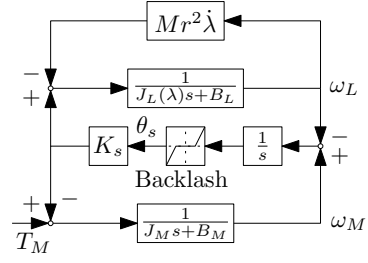
deadband. The longitudinal motion of the vehicle body is

$$M\frac{dv}{dt} = F - F_d, \tag{7}$$

where M, v, and F_d are the vehicle mass, vehicle speed, and air resistance, respectively. The driving force is $F = \mu(\lambda)N$ where N is the vehicle load, μ is the friction coefficient of the road surface, and λ is the slip ratio defined as

$$\lambda = \frac{v_\omega - v}{\max(v_\omega, v, \epsilon)}, \tag{8}$$

where v_ω is the wheel longitudinal speed which is calculated by $v_\omega = r\omega$, and ϵ is the small positive value which prevent zero division. The relationship between the slip ratio and the road friction coefficient μ is described by the magic formula proposed by Pacejka [15].

B. Drivetrain model

For the purpose of controller design, it is possible to neglect F_d, which is a disturbance term in (7). From (7) and the definition of (8) of the slip ratio, the driving force can be expressed as $F = M\dot{v} = Mr^2(1-\lambda)\dot{\omega}_L + Mr^2\dot{\lambda}\omega$. As presented in previous papers [11], [12], using this expression of F and equation (4), the rotational motion of the load side is also expressed as,

$$J_L(\lambda)\dot{\omega}_L = K_s\theta_s - B_L\omega_L - Mr^2\dot{\lambda}\omega, \tag{9}$$

$$J_L(\lambda) = J_{L0} + Mr^2(1-\lambda). \tag{10}$$

Based on the above equations, the drivetrain can be established as a two-inertia block diagram in Fig. 2, where λ and $\dot{\lambda}$ are considered as parameters. Hence, the respective transfer functions from the motor torque to the motor speed and wheel are obtained when the slip ratio is stable.

$$P_{Mn}(s) = \frac{\omega_M}{T_M} = \frac{J_L(\lambda)s^2 + B_Ls + K_s}{a_3(\lambda)s^3 + a_2(\lambda)s^2 + a_1(\lambda)s + a_0} \tag{11}$$

$$P_{Ln}(s) = \frac{\omega_L}{T_M} = \frac{K_s}{a_3(\lambda)s^3 + a_2(\lambda)s^2 + a_1(\lambda)s + a_0} \tag{12}$$

where a_3, a_2, a_1, a_0 are defined as $a_3(\lambda) = J_MJ_L(\lambda)$, $a_2(\lambda) = J_L(\lambda)B_M + J_MB_L$, $a_1(\lambda) = B_MB_L + J_MK_s + J_L(\lambda)K_s$, $a_0 = (B_M + B_L)K_s$. These parameters are obtained by system identification using chirp wave motor torque input when $\lambda = 1$.
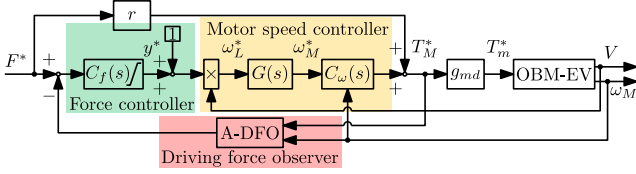
Fig. 3. Overall driving force controller.

Fig. 4. Adaptive driving force observer (A-DFO).

III. PROPOSED DFC SYSMTE

A. Outline of the control system

Define the variable,

$$y = \frac{v_\omega}{v} - 1. \tag{13}$$

It can be seen that

$$y = \begin{cases} \frac{\lambda}{1-\lambda} & (\lambda > 0), \\ \lambda & (\lambda < 0). \end{cases} \tag{14}$$

Thus, y almost equals to λ, especially when λ is close to 0. Linearizing the magic formula with small λ, we can treat y as the signal to control the driving force [10]. Let y^* be the output of the force controller, the reference speed of the wheel can be calculated as

$$\omega_L^* = v(1 + y^*) \tag{15}$$

From the transfer function $P_{Mn}(s)$ and $P_{Ln}(s)$, the transformation from ω_L to ω_M can be derived as

$$G_{M \to L}(s) = Q(s)P_{Ln}^{-1}(s)P_{Mn}(s) \tag{16}$$

where $Q(s) = 1/(\tau_Q s + 1)^3$ is a low-pass filter with the time constant of τ_Q. $Q(s)$ is introduced to make $G_{M \to L}(s)$ proper tranfer function.

Based on the above discussion, the block diagram of the proposed DFC system is established in Fig. 3 where $C_f(s)$ is the force controller. With respect to the nominal dynamics $F = D_s y$, C_f can be designed as an integral controller by pole placement: $C_f(s) = K_i/s$. The feedforward force control signal is realized by rF^* where F^* is the reference driving force. Besides, g_{md} is to transform form T_M^* to T_m^*. A-DFO represents the block diagram of the adaptive driving force observer and $C_\omega(s)$ is the speed controller. They will be designed in the following subsections.

B. Adaptive driving force observer

Based on (3) - (6), a state space model can be established to estimate four variables w_M, w_L, θ_s, and F simultaneously [16]. The goal of this paper is to demonstrate the adaptive estimation of the driving force by online identification of the viscous friction coefficient. For the sake of demonstration and implementation, this paper utilizes a reasonable assumption such that w_M and w_L are almost equal. Consequently, by summarizing (3) and (4), we have

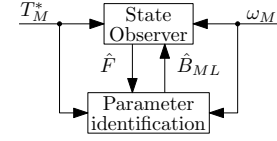$$J_{ML}\dot{\omega}_M = -B_{ML}\omega_M - rF + T_M \tag{17}$$

where $J_{ML} = J_M + J_{L0}$ and $B_{ML} = B_M + B_L$. Consequently, the following state space equation is obtained.

$$\begin{cases} \dot{X} = AX + BU \\ Y = CX \end{cases} \tag{18}$$

where the state vectors and matrics are defined as

$$X = \begin{bmatrix} \hat{\omega}_M & \hat{F} \end{bmatrix}^T, \ U = T_M, \ Y = \omega_M, \tag{19}$$

$$A = \begin{bmatrix} -\frac{B_{ML}}{J_{ML}} & -\frac{r}{J_{ML}} \\ 0 & 0 \end{bmatrix}, \ B = \begin{bmatrix} \frac{1}{J_{ML}} \\ 0 \end{bmatrix}, \ C = \begin{bmatrix} 1 \\ 0 \end{bmatrix}. \tag{20}$$

The continuous time state space model is transformed into the discrete-time model as

$$\begin{cases} X_{k+1} = A_d X_k + B_d U_k \\ Y_k = C_d X_k \end{cases} \tag{21}$$

where k is the time step index, and $A_d \simeq (I + AT_s)$, $B_d \simeq BT_s$, $C_d = C$, I is the 2×2 unity matrix. T_s is the sampling time which is small enough such that the aforementioned approximation of A_d and B_d are acceptable ($T_s = 1\,\text{ms}$ in this study).

The pair of $(A_d, \ C_d)$ is observable with the non-zero values of J_{ML} and B_{ML}. Thus, it is possible to estimate the driving force using the torque command of T_m and the measurement of ω_M. The inertia terms can be calculated from the geometry of the drivetrains's mechanical system. However, the viscous friction coefficients depend on torque transmission efficiency, and it is very hard to know these values accurately. To deal with the influence of friction coefficient uncertainty, this paper utilizes the A-DFO with the configuration shown in Fig. 4. The A-DFO consists of a state observer and a parameter identification. The state observer is designed as:

$$\hat{X}_{k+1} = \hat{A}_{d,k}\hat{X}_k + B_d U_k + L_d(Y_k - C_d\hat{X}_k) \tag{22}$$

where L_d is designed by pole placement to the estimation error dynamics using the initial value of the parameters J_{ML} and B_{ML}. Matrix $\hat{A}_{d,k}$ is updated at every estimation period as

$$\hat{A}_{d,k} = I + \begin{bmatrix} -\frac{\hat{B}_{ML,k}}{J_{ML}} & -\frac{r}{J_{ML}} \\ 0 & 0 \end{bmatrix} T_s \tag{23}$$

where $\hat{B}_{ML,k}$ is sent from the parameter identification, which will be described in the following part. From equation (22), we have:
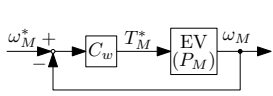
$$\phi^T \theta = \gamma \tag{24}$$

Fig. 5. Motor speed controller block diagram.
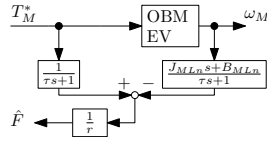

Fig. 6. Conventional DFO.

where $\theta = B_{ML}$, $\phi^T = \omega_M$, $\gamma = T_M - J_{ML}\dot{\omega}_M - rF$. Consequently, the parameter θ is identified by the RLS algorithm [10].

$$\hat{\theta}_k = \hat{\theta}_{k-1} + K_k(\gamma_k - \phi_k^T\hat{\theta}_{k-1}) \qquad (25)$$

$$K_k = P_{k-1}\phi_k(\sigma + \phi_k^T P_{k-1}\phi_k)^{-1} \qquad (26)$$

$$P_k = \frac{1}{\sigma}(I - K_k\phi_k^T)P_{k-1} \qquad (27)$$

where σ is the forgetting factor, which is slightly close to 1. Besides, γ is updated at every estimation period using the estimated driving force sent from the state observer.

$$\gamma_k = T_{M,k} - J_{ML,k}\dot{\omega}_{M,k} - r\hat{F} \qquad (28)$$

In order to guarantee the convergence of the A-DFO, the state estimation gain and the forgetting factor should be selected for faster convergence of driving force estimation while considering the effect of noise. The RLS algorithm is not used until the motor speed exceeds a threshold value ω_{th} for stable estimation.

C. Proposal of high order motor speed control

In the conventional method [11], the PI controller $C_{w,pi}$ is designed assuming that the differential gear is a rigid body. The pole placement for the closed loop system is conducted by the plant $P_n = 1/((J_M + J_{L0})s)$.

$$C_{w,pi} = k_p + \frac{k_i}{s} \qquad (29)$$

However, to make the plant model close to the actual drivetrain, the two-inertia model P_{Mn} is used as the control plant in the proposed DFC as shown in Fig. 5. As a proposed motor speed controller, a PID controller and phase lead compensator are used, and they are defined as

$$C_{w,pid-lead} = \left(k_p + \frac{k_i}{s} + \frac{k_d s}{\tau_d s + 1}\right)\left(\frac{\tau_1 s + 1}{\tau_2 s + 1}\right)$$
$$= \frac{b_3 s^3 + b_2 s^2 + b_1 s^1 + b_0}{s^3 + c_2 s^2 + c_1 s}. \qquad (30)$$

The plant P_{Mn} and $C_{w,pid-lead}$ are third-order, and the characteristic polynomial equation of the closed loop system is sixth-order. The number of control parameters b and c is six, and the linear equation for pole placement of the closed loop system can be solved. The phase lead compensator increases the FB bandwidth while increasing the phase margin. Thus, the proposed DFC uses the PID controller and phase lead compensator $C_{w,pid-lead}$ instead of the PI controller $C_{w,pi}$ as the motor speed controller.

TABLE I
VEHICLE PARAMETERS.

Parameter	Value
J_M	$1.55\,\text{kgm}^2$
J_{L0}	$1.24\,\text{kgm}^2$
B_M	$3.1\,\text{Nms/rad}$
B_L	$0\,\text{Nms/rad}$
K_s	$2784\,\text{Nm/rad}$
M	$925\,\text{kg}$
r	$0.301\,\text{m}$

IV. SIMULATION

A. Evaluation Setting

The main parameters of the vehicle are summarized in Table I. The value of viscous friction coefficient B_M in the actual plant is 3.1, however considering the modeling error, the nominal values of B_{Mn} are 4 in the simulation and 2.5 in the HIL experiment to confirm the effectiveness of the proposed method.

The proposed speed controller $C_{w,pid-lead}$ and A-DFO are compared with the conventional speed controller $C_{w,pi}$ and DFO as shown in Fig. 6. The following three types of controllers are compared. Firstly as the conventional method (Conv.), DFO with $B_{MLn} = 0$ and PI controller $C_{w,pi}$ are used. Secondly, as the extension of the conventional method (Prop1), viscous friction is considered in the conventional DFO, and the high-order speed controller $C_{w,pid-lead}$ is selected. Finally, the combination of A-DFO and $C_{w,pid-lead}$ is the second proposal of DFC (Prop2).

The parameters of $C_{w,pi}$ are $k_p = 59.95$, $k_i = 164.85$, and those of $C_{w,pid-lead}$ are $k_p = 138$, $k_i = 6$, $k_d = 0.6$, $\tau_d = 0.004$, $\tau_1 = 0.005$, $\tau_2 = 0.001$. The force controller gain K_i is set to 0.0005. The time constants of the conventional DFO and the transformation from w_L to w_M are set to 0.07 and 0.12, respectively. The poles of the state estimator are set to $[-400, -1000]^T$ and the forgetting factor σ and threshold motor speed ω_{th} are set to 0.99999 and 0.001, respectively.

B. Evaluation of overall DFC system

As an evaluation of the overall DFC, the tracking performance and estimation accuracy of Conv., Prop1, and Prop2 are compared. Figs. 7(a), 7(b), and 7(c) show the step reference of the driving force, the actual driving force, and the estimation results. The gap between the actual and the estimated driving force is the estimation error. As the speed increases, the estimation error of the Conv. increases due to the effect of viscous friction. While Prop1 reduces the estimation error, the influence of modeling error remains an issue. On the other hand, the effect of modeling error is eliminated by using Prop2. Fig. 7(d) shows the results of viscous friction estimation, and it is properly estimated by RLS. The difference of reference and the actual driving force are compared to evaluate the tracking performance. Although it is heavily influenced by estimation accuracy, the vibration of about $0.2\,\text{Hz}$ is eliminated by using $C_{w,pid-lead}$.
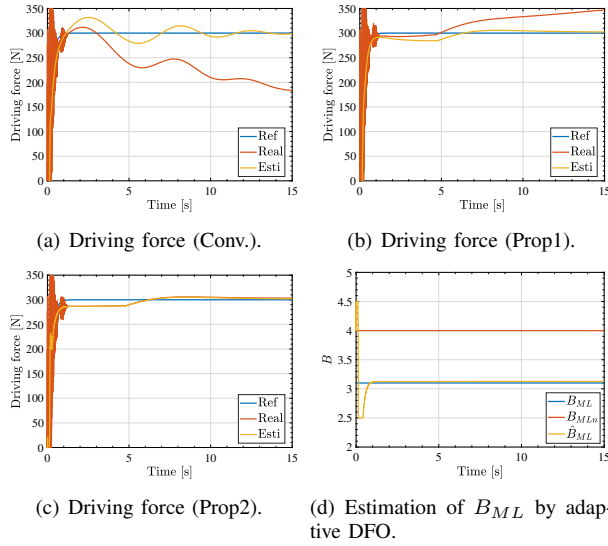
(a) Driving force (Conv.).

(b) Driving force (Prop1).

(c) Driving force (Prop2).

(d) Estimation of B_{ML} by adaptive DFO.

Fig. 7. Simulation of overall DFC.

Fig. 8. Hardware-in-loop experiments setup.

(a) Nyquist plot.

(b) Enlarged Nyquist plot.

(c) Sensitivy function.

(d) Tracking performance.

Fig. 9. Motor speed control comparison.

(a) Conv. without B.

(b) Conv. with B.
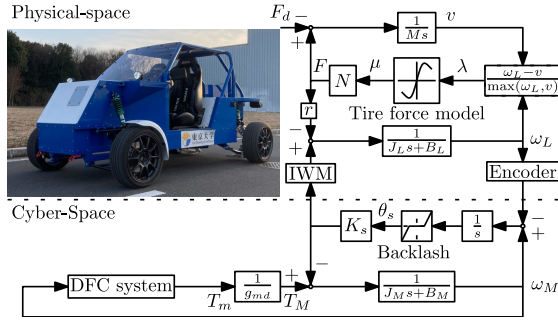

(c) A-DFO.

(d) Viscous friction estimation.
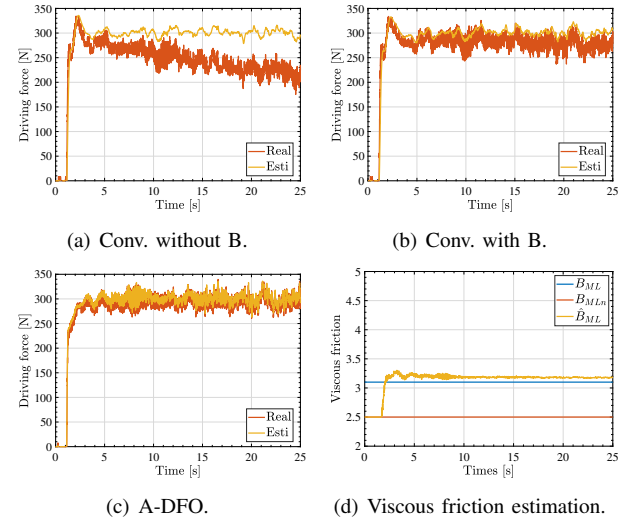
Fig. 10. Evaluation of driving force observer.

V. EXPERIMENT

A. Experimental system

To evaluate the proposed method, an experimental vehicle FPEV5 driven by rear-left-IWM is used. As shown in Fig. 8, the load side of the two-inertia system is real IWM, and real-time simulation is performed from the motor to the differential. This configuration enables the evaluation of the controller for OBM-EVs using IWM-EVs. To confirm HIL experiments, the results of simulations and HIL experiments are also compared.

The motor speed controller and DFO are independently validated. The evaluation of overall DFC is compared with Conv, Prop1, and Prop2 as in the simulation. In the HIL experiments, the force controller integral gain K_i, forgetting factor σ and motor speed threshold ω_{th} for RLS are set to 0.000375, 0.9964, and 0.2, respectively.

B. Evaluation of motor speed control

The tracking performance to the speed reference is compared with $C_{w,pi}$ and $C_{w,pid-lead}$. The Nyquist plots of the systems as shown in Figs. 9(a) and 9(b) show that the propose method increase the phase margin. $C_{w,pi}$ designed by the simple inertia plant P_n has a peak in the sensitivity function in the real system P_{Mn}, and the peak around $0.2\,\mathrm{Hz}$
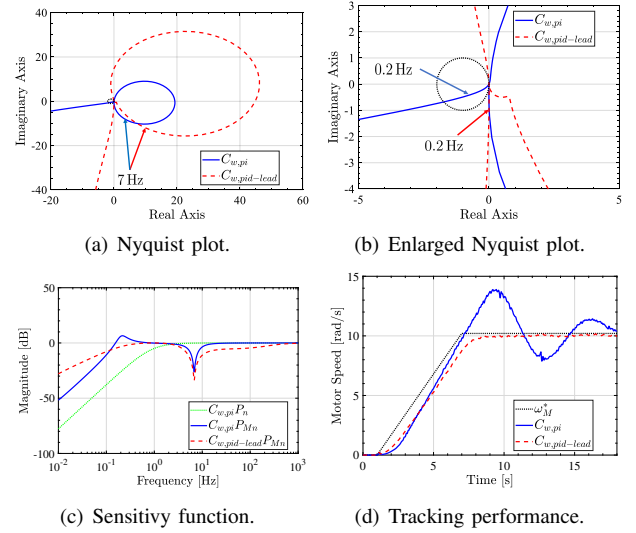
is suppressed by $C_{w,pid-lead}$. The reference and measured motor angular speed are shown in Figs 9(d). The proposed controller $C_{w,pid-lead}$ eliminates both overshoot and $0.2\,\mathrm{Hz}$ vibration.

C. Evaluation of driving force ovserver

DFO is compared with conventional DFO and A-DFO when $C_{\omega,pid-lead}$ is used as motor speed controllers. Figs. 10(a), 10(b), and 10(c) show the reference and actual driving force of three types of DFO. Since HIL experiments use IWM-EVs, the actual driving force is calculated by $\hat{F}_{real} = (K_s\theta_s - J_{L0}\dot{\omega}_L)/r$. Proposed A-DFO can estimate viscous friction coefficient as shown in Fig. 10(d). The root-mean-square-error (RMSE) values between the estimation and actual driving force in simulation and experiment are shown in Fig. 12(a). The estimation error is greatly reduced by using A-DFO.
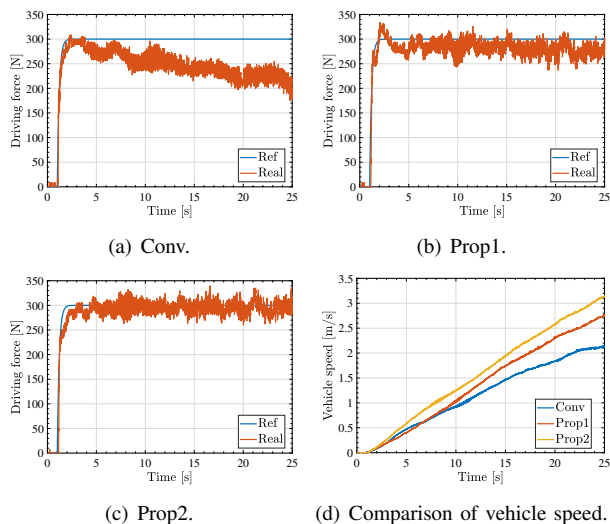
(a) Conv.

(b) Prop1.

(c) Prop2.

(d) Comparison of vehicle speed.

Fig. 11.   Evaluation of the overall DFC system.
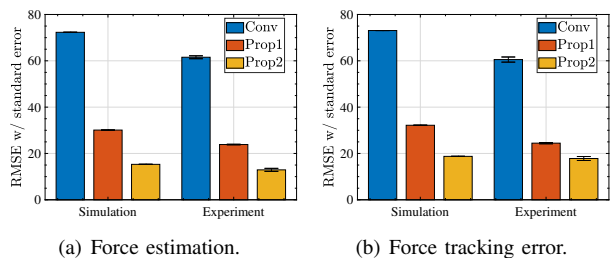

(a) Force estimation.

(b) Force tracking error.

Fig. 12.   RMSE evaluation of the proposed system.

D. Evaluation of overall DFC

The overall driving force is evaluated by comparing the tracking errors of Conv, Prop1, and Prop2. Figs. 11(a), 11(b), and 11(c) show the reference and actual driving force. The RMSE values of tracking error in simulation and experiment are shown in Fig. 12(b). The tracking error is reduced by the proposed method. Fig. 11(d) shows the comparison of vehicle speed of these methods. For vehicle acceleration, it is important to estimate the viscous friction coefficient. The response and RMSE values are similar between simulation and HIL experiments, thus the validity of the HIL experiments is confirmed.

VI. CONCLUSION

We propose a DFC that integrates A-DFO and the high order speed controller for OBM-EVs. This controller effectively addresses the challenges related to vibrations and driving force estimation error when using DFC for OBM-EVs. By Utilizing the high order speed controller which is designed to increase the phase margin for the two-inertia plant model, the vibration and overshoot are eliminated. The proposed A-DFO adequately estimates both the driving force and viscous friction coefficient simultaneously. The effectiveness of this method is verified by simulations and novel HIL experiments. By using HIL experiments, DFC for any type of EVs is evaluated by IWM-EVs. In future, we will extend the state space model of the A-DFO to

remove the assumption that $w_L = w_M$. The design of the feedforward controller and anti-windup feedback controller will be considered for the force control layer. Furthermore, we will implement and evaluate the proposed system using real OBM-EVs.

REFERENCES

[1] S. Oki and Y. Sato, "Nissan leaf and e-power: Evolution of motors and inverters," *IEEJ Journal of Industry Applications*, vol. 13, no. 1, pp. 8–16, 2024.

[2] L. Hua, J. Tang, H. Dourra, and G. Zhu, "A gray-box surrogate vehicle energy consumption model capable of real-time updating," *IEEE/ASME Transactions on Mechatronics*, vol. 28, no. 4, pp. 2092–2100, 2023.

[3] M. Hattori, O. Shimizu, S. Nagai, H. Fujimoto, K. Sato, Y. Takeda, and T. Nagashio, "Quadrant dynamic programming for optimizing velocity of ecological adaptive cruise control," *IEEE/ASME Transactions on Mechatronics*, vol. 27, no. 3, pp. 1533–1544, 2022.

[4] Y. Hosomi, B.-M. Nguyen, S. Nagai, and H. Fujimoto, "Learning-based distributed approach to energy-optimized speed trajectory for electric vehicles at multiple signalized intersections," in *IECON 2023-49th Annual Conference of the IEEE Industrial Electronics Society*, pp. 1–6, 2023.

[5] T. Liu, K. Tan, W. Zhu, and L. Feng, "Optimal and adaptive engine switch control for a parallel hybrid electric vehicle using a computationally efficient actor-critic method," in *2023 IEEE/ASME International Conference on Advanced Intelligent Mechatronics (AIM)*, pp. 416–423, 2023.

[6] V. Beliautsou, J. Alfonso, J. Giltay, F. Buchner, B. Shyrokau, J. A. Castellanos, and V. Ivanov, "Validation of integrated ev chassis controller using a geographically distributed x-in-the-loop network," in *2022 IEEE Vehicle Power and Propulsion Conference (VPPC)*, pp. 1–7, 2022.

[7] T. Suzuki, M. Mae, T. Takeuchi, H. Fujimoto, and E. Katsuyama, "Model-based filter design for triple skyhook control of in-wheel motor vehicles for ride comfort," *IEEJ Journal of Industry Applications*, vol. 10, no. 3, pp. 310–316, 2021.

[8] B.-M. Nguyen, J. P. F. Trovao, M. C. Ta, and M. Kawanishi, "Longitudinal motion control of electric vehicles: Glocal model and design using passivity," *IEEE Vehicular Technology Magazine*, vol. 16, no. 3, pp. 75–86, 2021.

[9] D. Savitski, V. Ivanov, K. Augsburg, T. Emmei, H. Fuse, H. Fujimoto, and L. M. Fridman, "Wheel slip control for the electric vehicle with in-wheel motors: Variable structure and sliding mode methods," *IEEE Transactions on Industrial Electronics*, vol. 67, no. 10, pp. 8535–8544, 2020.

[10] H. Fujimoto, J. Amada, and K. Maeda, "Review of traction and braking control for electric vehicle," in *2012 IEEE Vehicle Power and Propulsion Conference*, pp. 1292–1299, 2012.

[11] H. Sumiya and H. Fujimoto, "Driving force control method using suppression control of driving-shaft vibration for electric vehicle with on-board motor," in *IEEJ Industry Applications Society Conf*, no. 106, pp. 115–120, 2012 (in Japanese).

[12] H. Fujimoto, T. Miyajima, and J. Amada, "Development of electric vehicle with variable drive unit system," in *International Electric Vehicle Technology Conference & Automotive Power Electronics Japan*, vol. 2014, 2014.

[13] Z. Li, L. He, Z. Shi, Y. Wei, M. Wang, and Q. Shi, "A sliding mode predictive control approach for traction control of battery electric vehicle," in *2022 6th CAA International Conference on Vehicular Control and Intelligence (CVCI)*, pp. 1–4, 2022.

[14] A. Scamarcio, C. Caponio, M. Mihalkov, P. Georgiev, J. Ahmadi, K. M. So, D. Tavernini, and A. Sorniotti, "Predictive anti-jerk and traction control for v2x connected electric vehicles with central motor and open differential," *IEEE Transactions on Vehicular Technology*, vol. 72, no. 6, pp. 7221–7239, 2023.

[15] H. B. Pacejka and E. Bakker, "The magic formula tyre model," *Vehicle system dynamics*, vol. 21, no. S1, pp. 1–18, 1992.

[16] S. Yamada and H. Fujimoto, "Vibration suppression control for a two-inertia system using load-side high-order state variables obtained by a high-resolution encoder," in *IECON 2014 - 40th Annual Conference of the IEEE Industrial Electronics Society*, pp. 2897–2903, 2014.